

Simultaneous, common-volume lidar observations and theoretical studies of correlations among Fe/Na layers and temperatures in the mesosphere and lower thermosphere at Boulder Table Mountain (40°N, 105°W), Colorado

Wentao Huang,¹ Xinzhao Chu,¹ Chester S. Gardner,² Zhangjun Wang,³ Weichun Fong,¹ John A. Smith,¹ and Brendan R. Roberts¹

Received 28 January 2013; revised 2 July 2013; accepted 17 July 2013; published 15 August 2013.

[1] Simultaneous and common-volume observations of Fe density, Na density, and temperatures in the mesosphere and lower thermosphere were made for 12 nights with an Fe Boltzmann lidar and a Na Doppler lidar at the Table Mountain Lidar Facility (40.13°N, 105.24°W) near Boulder, Colorado, in August and September 2010. We derive the correlations among temporal variations of Fe/Na densities and temperatures, eliminating the covariance bias via computing the cross correlations between Fe (Na) density and Na (Fe) temperature perturbations. The Fe-Na density correlation is positive below the Fe layer peak and above the Na peak where the Fe/Na density gradients have the same signs but becomes negative in between the Fe and Na peaks where the gradients are opposite. The large correlation between temperature and density fluctuations is positive on the layer bottomside but negative on the topside with the transitions occurring near the layer peaks. The relative Fe/Na variances reach minimum near the layer peaks but rapidly increase and exceed the relative temperature variance significantly toward edges. These observations can be largely reproduced by theoretically modeling the metal layer responses to the wave-induced perturbations only through dynamic processes with a Gaussian stationary density distribution. These results suggest that the dynamic effects (mainly the vertical displacement) induced by gravity waves or tides dominate the observed short-term density and temperature variations over a night. We explain the Fe/Na gradient difference observed at the bottomside via the chemical “shelf” around 80 km for reactive chemicals and the Fe/Na layer height difference.

Citation: Huang, W., X. Chu, C. S. Gardner, Z. Wang, W. Fong, J. A. Smith, and B. R. Roberts (2013), Simultaneous, common-volume lidar observations and theoretical studies of correlations among Fe/Na layers and temperatures in the mesosphere and lower thermosphere at Boulder Table Mountain (40°N, 105°W), Colorado, *J. Geophys. Res. Atmos.*, *118*, 8748–8759, doi:10.1002/jgrd.50670.

1. Introduction

[2] The Earth’s metal layers (Fe, Na, K, Ca, and Li) in the mesosphere and lower thermosphere (MLT) originate from meteor ablation [Plane, 2003]. These metals can be observed with ground-based lidars (see a summary by Chu and Papen [2005]), providing not only their density but also temperature

and wind measurements. The metal layers are affected by complex dynamical and chemical processes in the MLT region. Wave-induced vertical transport of atmospheric species through mixing, displacement, and advection [Gardner and Liu, 2010], in combination with chemistry and meteor input [Plane, 2012] as well as (horizontal) meridional transport [Marsh, 2011; Gardner et al., 2005], controls the abundance and structure of the metal layers in the MLT. While advective transport (upward in summer and downward in winter) is important in the seasonal variations of metal layers, eddy transport, dynamical transport, and chemical transport play crucial roles in the short-term (within a night) temporal variations of metal layer density [Gardner and Liu, 2010]. Eddy transport occurs through the turbulent mixing generated by breaking waves and tides. Dynamic transport results from the net vertical displacement of the metal species caused by dissipating but nonbreaking gravity waves. Nondissipating gravity waves can also displace the metals when the waves propagate through the layers, but the net displacement, averaged over

¹Cooperative Institute for Research in Environmental Sciences and Department of Aerospace Engineering Sciences, University of Colorado Boulder, Boulder, Colorado, USA.

²Department of Electrical and Computer Engineering, University of Illinois at Urbana-Champaign, Urbana, Illinois, USA.

³Institute of Oceanographic Instrumentation, Shandong Academy of Sciences, Qingdao, China.

Corresponding author: X. Chu, Cooperative Institute for Research in Environmental Sciences and Department of Aerospace Engineering Sciences, University of Colorado Boulder, 216 UCB, Boulder, CO 80309, USA. (Xinzhao.Chu@colorado.edu)

the wave period, is zero. Chemical transport is induced when the waves or tides alter the chemical reactions (production and/or loss) involving the metal species. Advective and dynamical transports, as well as the vertical displacement caused by nondissipating gravity waves, induce the same physical movement in all the constituents in an air parcel. Eddy and chemical transports vary between different species because their background profiles and chemistry are different.

[3] Simultaneous and common-volume observations of multiple species are invaluable for understanding these transport processes and validating metal chemistry models [Helmer *et al.*, 1998; Plane *et al.*, 1999]. Unfortunately, observations of multiple species are rare, although general properties of Fe and Na layers have been reported by several groups independently [Tilgner and von Zahn, 1988; Plane *et al.*, 1999; States and Gardner, 1999; Raizada and Tepley, 2003; Gardner *et al.*, 2011] and by a few correlative observations [Kane and Gardner, 1993; Gardner *et al.*, 1993, 2005]. The lidar group at Wuhan has undertaken extensive simultaneous Fe and Na observations with broadband resonance lidars [Yi *et al.*, 2008, 2009]. Several unique features have been characterized from a large amount of data [Chen and Yi, 2011; Ma and Yi, 2010], but definitive explanations for these features are still lacking. Due to the lack of temperature measurements, these studies at Wuhan have not investigated the correlation between the constituent density and temperature perturbations in the MLT.

[4] Although chemistry is an important factor in establishing the structure of the Fe and Na layers, under most conditions, the observed short-term density fluctuations appear to be dominated by dynamical effects [Plane *et al.*, 1999; Plane, 2003]. The first attempt to characterize the wave-induced fluctuations of a neutral, chemically inert constituent layer was published by Chiu and Ching [1978]. They used a perturbation series analysis of the continuity equation and the gravity wave polarization relations to compute the linear response to a monochromatic wave and applied the results to the stratospheric ozone layer. Gardner and Shelton [1985] extended the analysis by deriving an exact solution for the fluctuations of neutral constituent layers caused by a monochromatic gravity wave, which they used to analyze Na layer fluctuations. Most recently, Gardner and Liu [2010] generalized the results by eliminating the gravity wave constraint and extending the calculations to a full spectrum of wind fluctuations. They obtained solutions for the temperature-constituent covariance function and the vertical constituent flux, which include both linear and nonlinear perturbation effects. However, so far, there have not been any theoretical studies of the covariance between different constituents in the MLT under the same wave perturbations.

[5] A unique opportunity came along to expand simultaneous Fe and Na studies to include correlations among the Fe/Na layer densities and temperatures in the MLT, theoretical derivation of the covariance between the Fe and Na density perturbations, and comparisons to observations, when the University of Colorado lidar group conducted a campaign at Boulder in 2010. In August and September 2010, we made 59 h of simultaneous and common-volume observations of mesospheric Fe/Na layers and MLT temperatures during 12 nights at the Table Mountain Lidar Facility (40.13°N, 105.24°W) located north of Boulder, Colorado,

with two resonance fluorescence lidars. These new data from North America enable various new investigations, such as thermospheric metal layers, correlations among the Fe/Na layer densities and temperatures, and layer boundary correlation. In the current work, we mainly focus on the correlation among the Fe density, Na density, and temperatures in the MLT (section 4) with both observational and theoretical modeling studies. In section 5, we investigate the Fe and Na density gradients in the layer boundary correlation, make comparisons to the Wuhan observations, and provide a plausible explanation. The lidar campaign at Boulder in 2010 is introduced in section 2, and observed general layer features are given in section 3. The study is concluded with new science findings and results.

2. Boulder Campaign 2010

[6] From July to September 2010, an Fe Boltzmann temperature lidar and a Na Doppler wind and temperature lidar were operated side by side at the Table Mountain Lidar Facility near Boulder, Colorado. Originally developed at the University of Illinois 15 years ago [Chu *et al.*, 2002], the Fe Boltzmann lidar consists of two independent, vertical-pointing channels probing the 372 and 374 nm absorption lines of neutral Fe atoms, respectively. The ratios between these two channels are used to derive the Fe temperature in the MLT region by employing the Boltzmann technique [Gelbwachs, 1994; Chu *et al.*, 2002]. Over the last decade, this lidar has been deployed to the Pacific Ocean, the North Pole, the South Pole, and Rothera, Antarctica, under harsh environment [Chu *et al.*, 2000; Gardner *et al.*, 2001, 2005, 2011], so we must refurbish and upgrade the lidar to restore and enhance its capabilities before deploying it to McMurdo, Antarctica, in November 2010 [Chu *et al.*, 2011a]. Such refurbishment and upgrade along with extensive sky tests were conducted at the University of Colorado [Z. Wang *et al.*, 2012], which led to the Boulder observations in 2010. The divergence angles of the two lidar beams were ~ 0.35 mrad, producing spots of 35 m in diameter at the altitude of 100 km. Raw data were taken in 48 m and 1 min resolutions.

[7] The *Student Training and Atmospheric Research (STAR)* lidar is a Na Doppler system. It was constructed by graduate students at the University of Colorado in summer 2010 [Smith *et al.*, 2012]. Originally intended for student training purposes, its scientific research values were quickly recognized as demonstrated by this study. This lidar is similar in design to the classical dye-laser-based Na Doppler lidar systems developed by the Colorado State University (CSU) and the University of Illinois at Urbana-Champaign (UIUC) lidar groups (see summaries by Arnold and She [2003] and by Chu and Papen [2005]). A slight difference is that the frequency shifts by the dual acoustic-optic modulators are ± 480 MHz, instead of ± 630 MHz employed by the CSU and UIUC groups [Smith *et al.*, 2012]. By employing the three-frequency technique to probe the Na D_{2a} line, the temperature, line of sight wind, and Na density can be derived simultaneously [Chu and Papen, 2005]. One vertical-pointing beam (switching among three frequencies) of 0.8 mrad divergence was employed for this research, producing a spot of ~ 80 m in diameter at 100 km altitude. A vertical-pointing 40 cm Cassegrain telescope was employed in this receiver

Table 1. Mean Values and Standard Deviations of Fe and Na Layer Characteristics at Boulder in August and September 2010^a

Mean Characteristics	Fe	Na
Column abundance (10^9 cm^{-2})	10.65 ± 3.40	3.45 ± 1.62
Centroid altitude (km)	89.66 ± 1.05	92.04 ± 0.81
RMS width (km)	4.38 ± 0.59	4.23 ± 0.52
Peak density (10^3 cm^{-3})	13.03 ± 3.34	3.85 ± 1.78
Peak altitude (km)	86.82 ± 1.51	92.08 ± 2.36

^aSimultaneous observations were made on 7, 11, 13, 14, and 18 August 2010 and on 2, 3, 4, 5, 12, 14, and 15 September 2010.

configuration to collect the 2010 data used in this study. The raw data were taken in 96 m and 30 s resolutions.

[8] Based on their unique measurement principles and system designs, these two lidars were independently calibrated. The Fe Boltzmann lidar was calibrated with the approach outlined in *Chu et al.* [2002] by scanning the laser frequencies through the absorption lines of Fe atoms in the MLT region. For the Na Doppler lidar, we measure the spectrum and line shape of the outgoing laser pulses in the laboratory using a scanning Fabry-Perot interferometer and then incorporate the laser line shape information into the data retrieval process as demonstrated by *She et al.* [1992]. After the calibrations, the temperatures measured by these two lidars are comparable, and detailed comparisons in two nights will be shown in section 4.1. Though the Fe lidar had full-diurnal measurement capability, the Na lidar could only be operated at night. Consequently, only nighttime observations are included in this study. The two lidars were located 25 m apart and probed overlapping volumes of the MLT region. Raw data from both lidars were first integrated to the same 96 m and 5 min resolutions for density comparisons and then to 960 m and 15 min resolutions to achieve adequate signal-to-noise ratios for calculations involving measured temperature (the Fe and Na data are integrated to the same time and altitude grids). The processed data are truncated to cover Fe

and Na simultaneously with identical start and end times for each night. Twelve nights (59 h in total) of simultaneous density and temperature measurements made during the campaign in August and September 2010 are included in this study.

3. Lidar Observations

[9] The mean characteristics of Fe and Na layers during our observation period are summarized in Table 1. The Fe layer is lower and has a higher abundance than the Na layer while the widths of the two layers are comparable. These mean characteristics are similar to those that have been reported at other midlatitude sites in late summer and early autumn, e.g., the Fe and Na observations at Urbana (40°N) by *Kane and Gardner* [1993] and *States and Gardner* [1999], the Fe and Na observations at Wuhan (30°N) by *Yi et al.* [2009], and the Na observations at Fort Collins (41°N) by *She et al.* [2000].

[10] Simultaneous observations of Fe and Na density contours are plotted in Figure 1 for two representative nights (4 and 5 September 2010). The metal layers consist of many features that change through the night, and some appear differently in the Fe and Na contours. A double-peak feature occurs in the Na main layer (Figure 1b) on 4 September, but not in the Fe (Figure 1a). While the thermosphere descending or converged Fe layers above 100 km are obvious in Figures 1a and 1c, they are either much weaker or not obvious in the Na (Figures 1b and 1d). The main layer peak densities and shapes undergo large changes throughout these nights, especially in Figures 1b–1d.

[11] Because the centroid altitude of the Fe layer is several kilometers lower than that of the Na layer, the absolute density contours look quite different between Fe and Na as illustrated in Figure 1, which makes it hard to compare either absolute densities or absolute variations. However, the relative density perturbations plotted in Figure 2 reveal the

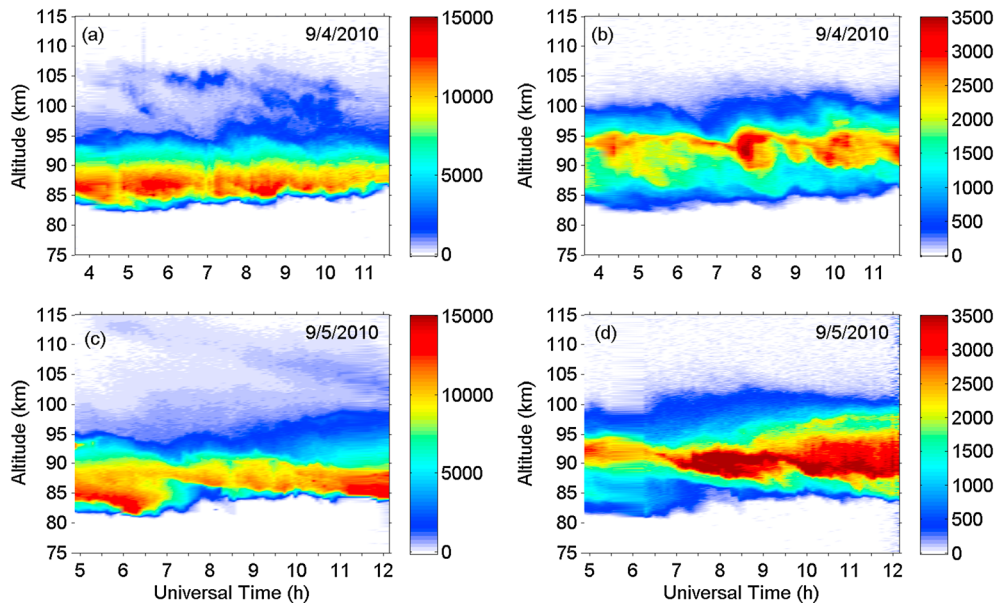


Figure 1. Contours of common-volume Fe and Na densities (unit: cm^{-3}) observed by two lidars simultaneously on (a, b) 4 September 2010 and (c, d) 5 September 2010. The temporal resolution is 5 min, and the vertical resolution is 96 m.

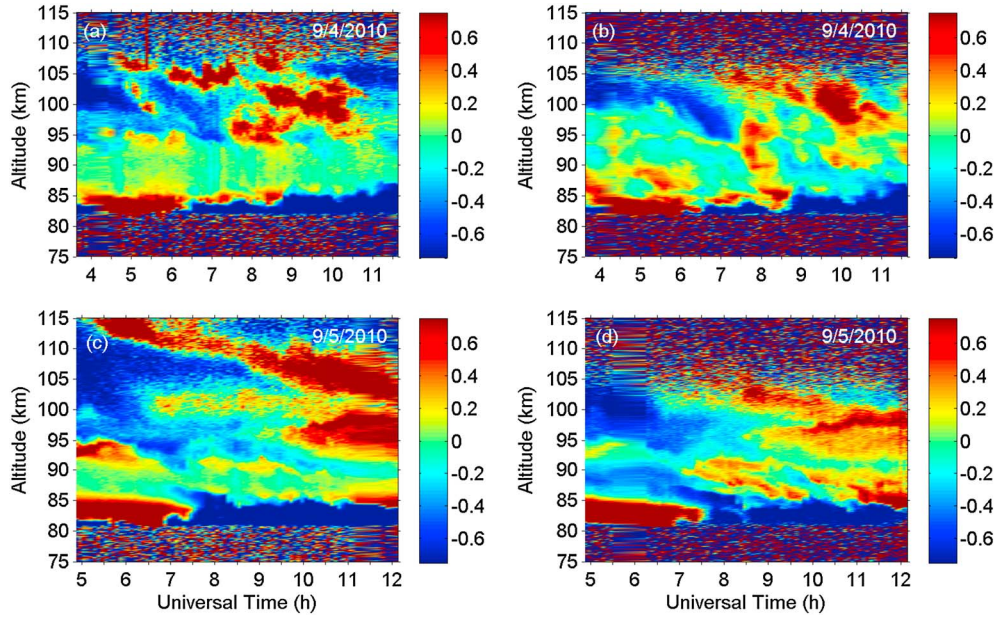


Figure 2. Contours of Fe and Na relative density perturbations on (a, b) 4 September 2010 and (c, d) 5 September 2010. The temporal resolution is 5 min, and the vertical resolution is 96 m.

correlated short-term density variations in both Fe and Na clearly. The relative Na density perturbation is defined as

$$\frac{\rho'_{\text{Na}}(z, t)}{\bar{\rho}_{\text{Na}}(z)} = \frac{\rho_{\text{Na}}(z, t) - \bar{\rho}_{\text{Na}}(z)}{\bar{\rho}_{\text{Na}}(z)}, \quad (1)$$

where $\rho_{\text{Na}}(z, t)$ is the absolute Na density at altitude z and time t , and $\bar{\rho}_{\text{Na}}(z)$ is the nightly mean density profile. The relative Fe density perturbation is defined similarly. In Figure 2, the Fe and Na layers exhibit similar temporal and spatial variations, including the thermosphere sporadic layers and many small-scale features. For example, the Fe and Na layers show similar patterns of larger density in earlier night but reduced density in later night near the bottomside (around and below 85 km) in both nights. From 8 to 10 UT on 4 September, the density enhancement around 100 km shows similar features between Fe and Na layers. On 5 September, an enhanced layer around 102 km appears in both Fe and Na observations spanning from 6.5 to 11 UT, while a density increase around 95 km from 9 to 12 UT is visible in both constituents with similar vertical extent. Another advantage of the relative density perturbations is to reveal the descending or converged Na layers above 100 km more clearly than in the absolute densities. For instance, the converged Na layer accompanying the descending Fe layer is clearly shown above 100 km in Figures 2a and 2b, but such Na layer is hardly seen in Figure 1b.

[12] We notice an interesting phenomenon from Figures 2c and 2d that a thermospheric Fe layer descends from 116 to 102 km across the night from 5 to 12 UT but such descending layer is missing from the Na observations in Figure 2d, although both Fe and Na exhibit converged but not descending layers around 102 km as discussed above. Through the Boulder campaign in 2010, seven out of 12 nights of observations exhibit thermospheric Fe descending or converged layers above 100 km, and most of them are accompanied with thermospheric Na layers. In the remaining five nights, neither Fe nor Na converged layer is above 100 km. In light

of the recent discovery of neutral Fe layers in the thermosphere up to 155 km at McMurdo, Antarctica [Chu *et al.*, 2011b], the thermosphere metal layers above 100 km become an interesting topic. Following the McMurdo discovery, Friedman *et al.* [2013] report a thermosphere K layer up to 150 km at Arecibo Observatory, Tsuda *et al.* [2012] report a thermosphere Na layer reaching 130 km at Syowa, Antarctica, and J. Wang *et al.* [2012] report an intensive Na layer up to 130 km at Beijing. Although the thermosphere descending or converged layers reported here are not as high as the events mentioned above, the simultaneous observations of thermosphere Fe and Na layers provide a different perspective than the single species observations in the aforementioned reports. So far, there are only two simultaneous observations of thermosphere Fe and Na layers: by Ma and Yi [2010] at Wuhan and the current study. A thorough investigation of the simultaneous observations of thermospheric Fe and Na layers at Table Mountain will be addressed in a separate paper.

4. Relationships Among the Fe, Na, and Temperature Perturbations

4.1. Observational Results

[13] The mean Fe, Na, and temperature profiles for 4 and 5 September 2010 are plotted in Figure 3. The Na and Fe profiles are typical of those expected for this time of year. Notice that the mean Fe layers on these nights exhibit secondary peaks in the thermosphere above 105 km altitude but these features are not obvious in the Na profiles. Both the Fe Boltzmann lidar and the Na Doppler lidar employed in this study are capable of profiling the MLT temperatures. The nightly mean temperatures measured by both lidars are compared in Figure 3 for both nights. In general, the temperature profiles are compared reasonably well between these two lidars: Fe temperatures have nearly identical profile shapes

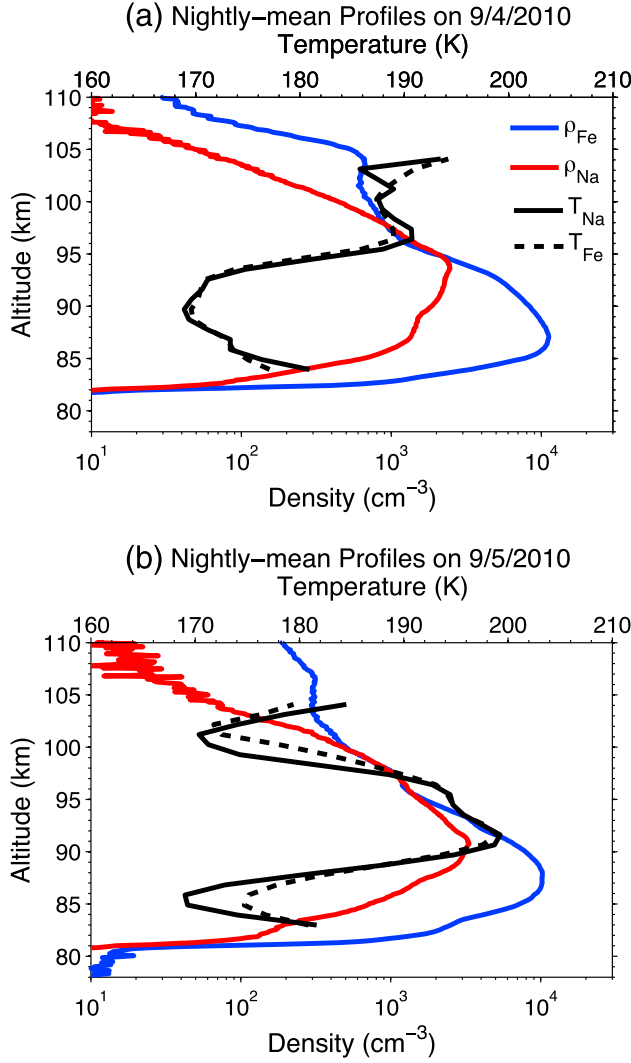


Figure 3. The nightly mean profiles of Fe density (blue), Na density (red), Na temperature (solid black), and Fe temperature (dashed black) on (a) 4 September and (b) 5 September 2010. The density nightly means are averaged from the density profiles with 5 min and 96 m resolutions through the nights, while the temperature nightly means are averaged from the temperature profiles with 15 min and 960 m resolutions. The nightly mean temperature errors are around 0.5 K at the layer peak and 1–3 K at the layer bottom (85 km) and top (100 km).

to Na temperatures in both nights, although the temperature shapes of these two nights are almost opposite around 90–95 km. The two lidar temperatures agree with each other in most of the altitude range. Some discrepancies exist but are mainly near the layer edges where the photon-noise-induced measurement errors increase substantially. The measured temperatures are typical of those expected for this time of year. The differences between the two nights are the result of tides and planetary waves. These mean density and temperature profiles will be used in the derivations of correlations and variances from the observational data and from the theoretical computation as shown below and in Appendix A.

[14] To quantify the relationships among Fe density, Na density, and temperature perturbations, we take the correlations

among these three measured quantities. For the measured perturbations, not only the real density/temperature perturbations induced by waves and chemistry processes contribute but also random fluctuations caused by photon noise are included. This situation can be expressed as the first equalities for temperature and density in equation (2):

$$\begin{aligned} T'_{\text{total}} &= T' + \Delta T = T(z, t) - \bar{T}(z) \\ \rho'_{c_{\text{total}}} &= \rho'_c + \Delta \rho_c = \rho_c(z, t) - \bar{\rho}_c(z), \end{aligned} \quad (2)$$

where T'_{total} and $\rho'_{c_{\text{total}}}$ are the total temperature and constituent density perturbations measured by the lidars, T' and ρ'_c are the wave- and chemistry-induced perturbations, and ΔT and $\Delta \rho_c$ are the photon-noise-induced random fluctuations, i.e., the error bars. The second equalities indicate how the total perturbations are derived from the observational data, where T and ρ_c are the measured temperature and constituent density at altitude z and time t , respectively, while \bar{T} and $\bar{\rho}_c$ are the mean temperature and density over the data sets at z , respectively. The desired correlations are among the pure perturbations induced by waves and chemistry processes (T' and ρ'_c), so we must correct the bias induced by the photon noise (ΔT and $\Delta \rho_c$) when calculating from the measured total perturbations (T'_{total} and $\rho'_{c_{\text{total}}}$).

[15] The correlation coefficient is the ratio of the covariance between two quantities to the product of standard deviations of these two quantities:

$$\begin{aligned} \text{Correlation}(T', \rho'_c) &= \frac{\langle T' \rho'_c \rangle}{\sqrt{\langle (T')^2 \rangle \langle (\rho'_c)^2 \rangle}} \\ &= \frac{\overline{T'_{\text{total}} \rho'_{c_{\text{total}}} - \Delta T \cdot \Delta \rho_c}}{\sqrt{[(T'_{\text{total}})^2 - (\Delta T)^2] [(\rho'_{c_{\text{total}}})^2 - (\Delta \rho_c)^2]}} \\ \text{Correlation}(\rho'_{\text{Fe}}, \rho'_{\text{Na}}) &= \frac{\langle \rho'_{\text{Fe}} \rho'_{\text{Na}} \rangle}{\sqrt{\langle (\rho'_{\text{Fe}})^2 \rangle \langle (\rho'_{\text{Na}})^2 \rangle}} \\ &= \frac{\overline{\rho'_{\text{Fe total}} \rho'_{\text{Na total}} - \Delta \rho_{\text{Fe}} \cdot \Delta \rho_{\text{Na}}}}{\sqrt{[(\rho'_{\text{Fe total}})^2 - (\Delta \rho_{\text{Fe}})^2] [(\rho'_{\text{Na total}})^2 - (\Delta \rho_{\text{Na}})^2]}}, \end{aligned} \quad (3)$$

where the overbars denote the data set means. Bias will be introduced to the variance in the denominator if the noise-induced fluctuations are large but not accounted for. In the numerator, bias can be also introduced to the covariance depending on whether the noise-induced fluctuations in the two quantities have correlations. Because the Fe and Na densities were measured from two independent lidars, the photon-noise-induced fluctuations in these two quantities were uncorrelated, leading to $\overline{\Delta \rho_{\text{Fe}} \cdot \Delta \rho_{\text{Na}}} = 0$. When T' and ρ'_c are derived from the same lidar measurements, ΔT and $\Delta \rho_c$ can be correlated and $\overline{\Delta T \cdot \Delta \rho_c}$ can have nonzero values. Fortunately, in our case, T' and ρ'_c can be derived from two independent lidars, so $\overline{\Delta T \cdot \Delta \rho_c}$ is zero. That is, to avoid the covariance bias, the T' - ρ'_c correlation will be computed between ρ'_{Na} and the Fe lidar measured T'_{Fe} , and between ρ'_{Fe} and the Na lidar measured T'_{Na} .

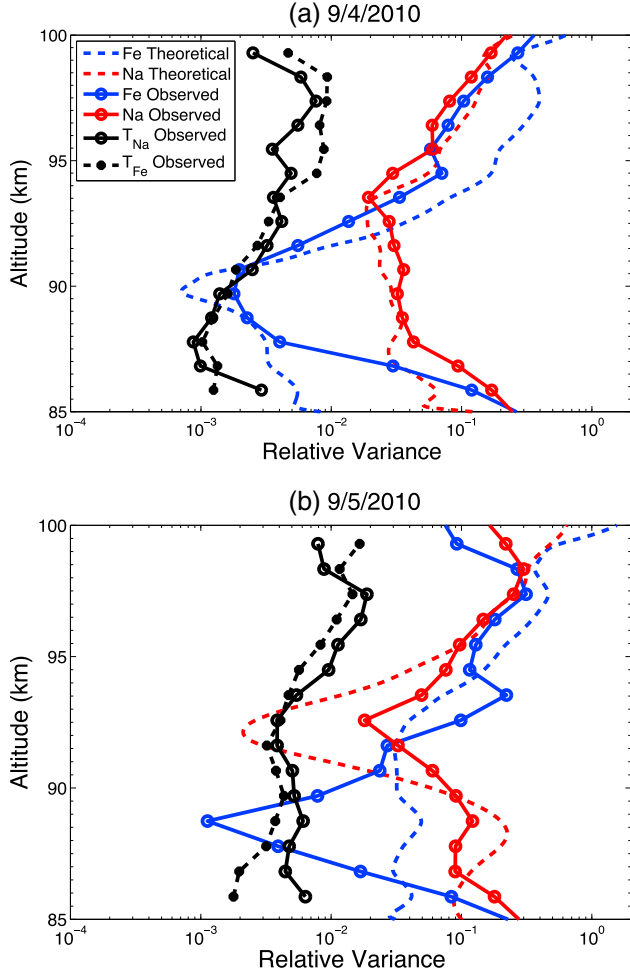


Figure 4. Theoretically calculated and lidar-observed relative variances of Fe and Na densities and lidar-observed relative variance of Na and Fe temperatures on (a) 4 September and (b) 5 September 2010 with 960 m and 15 min resolutions. Fe (Na) temperature is used in the theoretical calculation of Na (Fe) variance.

[16] The relative temperature and density variance profiles for the nights of 4 and 5 September 2010 are plotted in Figure 4. Here the relative variances are defined as

$$\frac{\text{Var}(T')}{\bar{T}^2} = \frac{(T'_{\text{total}})^2 - (\Delta T)^2}{\bar{T}^2} = \frac{[T(z, t) - \bar{T}(z)]^2 - [\Delta T(z, t)]^2}{\bar{T}(z)^2}$$

$$\frac{\text{Var}(\rho'_c)}{\bar{\rho}_c^2} = \frac{(\rho'_{c, \text{total}})^2 - (\Delta \rho_c)^2}{\bar{\rho}_c^2} = \frac{[\rho_c(z, t) - \bar{\rho}_c(z)]^2 - [\Delta \rho_c(z, t)]^2}{\bar{\rho}_c(z)^2}, \quad (4)$$

where the primes denote the perturbations and the overbars denote the data set means. A root-mean-square (RMS) value is defined as the square root of the relative variance. The Fe temperature variance is, in general, comparable to the Na temperature variance in both nights. Discrepancies are mainly near the layer edges where the temperature errors increase substantially, leading to larger uncertainties in the bias corrections. The relative temperature variance reaches a local minimum near 88 km on 4 September 2010, which

is very near the location of the mesopause (see Figure 3a). However, such minimum is not clear on 5 September 2010 when there is no clear location of mesopause averaging over the night (see Figure 3b). In general, the temperature variance increases with increasing altitude in both nights but with some uncertainties near the layer edges. Its RMS values range from about 3% or 5 K at 87.8 km altitude to ~10% or 18 K at 98.3 km on 4 September and from about 4% or 7 K at 85.9 km to ~13% or 23 K at 99.3 km on 5 September. The relative Fe variance on 4 September exhibits a local minimum with an RMS value of ~4% near 90 km altitude, about 3 km above the layer peak, and then increases rapidly with altitude reaching an RMS value of about 55% near 100 km. The variance also increases rapidly with decreasing altitude below the layer peak reaching an RMS value of ~35% near 86 km. The relative Fe variance on 5 September shows a similar overall profile with comparable RMS values as the previous night, but its minimum is located 1 km lower than in the previous night. The relative Na variance on 4 September exhibits a local minimum with an RMS value of ~14% near 94 km, around the layer peak, and then also increases with altitude reaching an RMS value of about 45% at 100 km, which is comparable to Fe. The relative Na variance near 86 km reaches an RMS value of ~41%, also comparable to Fe. The profile of the relative Na variance on 5 September is similar to that in the previous night with comparable RMS values but 1 km lower variance minimum. Near 100 km on the top edges of both layers, the Fe and Na RMS relative density perturbations are about 5 times larger than the RMS relative temperature perturbations in both nights. On the bottom edges of the layers near 86 km, the RMS Na and Fe perturbations are about 8 and 5 times larger than the temperature perturbations on 4 and 5 September, respectively.

[17] The correlations between the Fe density and Na temperature perturbations and between the Na density and Fe temperature perturbations are calculated using equation (3) and plotted in Figure 5 for the observations made on 4 and 5 September 2010. On the bottomsides of both layers, the correlation is large and positive, while on the topside, it is large but negative. The transitions between the positive and negative correlations occur several kilometers above the peaks of the Fe and Na layers. These results are similar to the annual mean T - ρ_c correlation profile reported by *Gardner and Liu* [2010] at the Starfire Optical Range, New Mexico (40°N). The overall T' - ρ'_c correlation profiles have quite comparable shapes between these two nights, but an obvious difference exists. That is, compared to those on 4 September, the transition points on 5 September are shifted down by about 2 km for both $T'_{\text{Na}}-\rho'_{\text{Fe}}$ and $T'_{\text{Fe}}-\rho'_{\text{Na}}$ correlations. As discussed above, the covariance bias is zero in our case because of the uncorrelated error terms from two independent lidar measurements, that is, $\overline{\Delta T_{\text{Na}} \Delta \rho_{\text{Fe}}} = \overline{\Delta T_{\text{Fe}} \Delta \rho_{\text{Na}}} = 0$. The variance bias is corrected by subtracting $(\Delta T)^2$ and $(\Delta \rho_c)^2$ from the total variance. Here ΔT and $\Delta \rho_c$ are computed as the RMS errors estimated from the photon noise [*Chu et al.*, 2002; *Gardner and Yang*, 1998].

[18] The correlations between the Fe and Na density perturbations for these same nights are calculated using equation (3) and plotted in Figure 6. Similar variance bias corrections are applied as discussed above. The data show robust positive correlations (>0.7) in the regions where the density

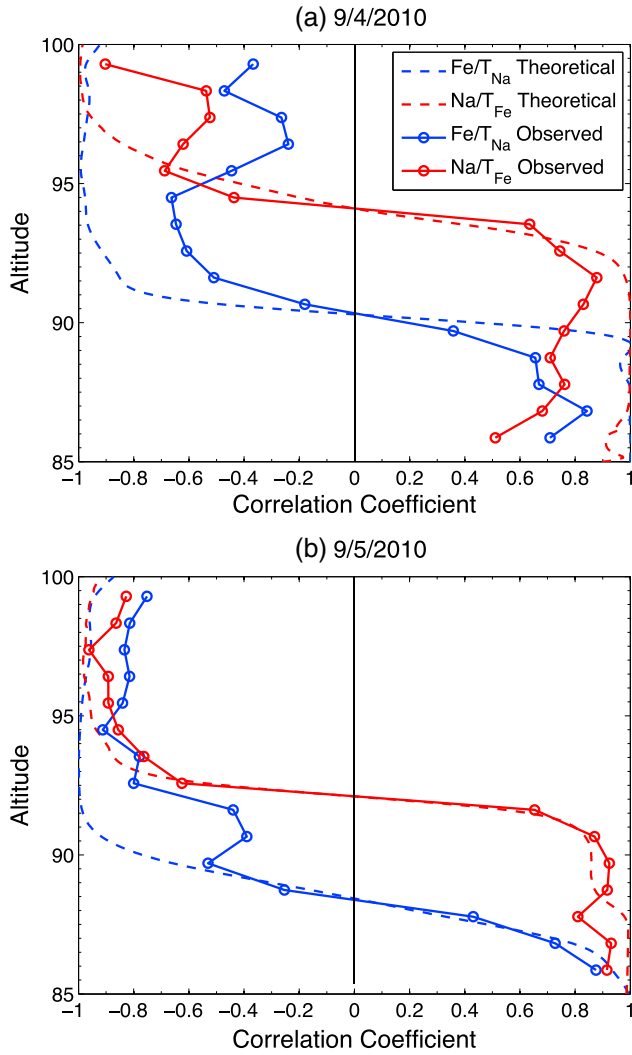


Figure 5. Theoretically calculated (dashed lines) and lidar-observed (solid lines) correlations between Fe (Na) density and Na (Fe) temperature perturbations on (a) 4 September and (b) 5 September 2010. Blue color is for Fe layers, while red color is for Na layers.

gradients of Fe and Na have the same signs, that is, the positive gradient region below the Fe layer peak and the negative gradient region above the Na layer peak. Significant negative correlations are seen within the altitude range where the Fe and Na density gradients are of the opposite signs, that is, between the Fe and Na peak altitudes. In other words, the Fe and Na density fluctuations are similar and in phase on the bottomsides and topsides of both layers and similar but 180° out of phase between the layer peaks. This behavior is similar to the observations reported by *Chen and Yi* [2011].

[19] The observed high correlations among the MLT temperature, Fe and Na density fluctuations are expected because these large fluctuations, at a given point and time, are induced by the same gravity waves and tides. In fact, previous observations have shown that the associated correlation coefficients among temperature, Fe and Na densities are often quite high (absolute values greater than 0.7) but the sign can vary rapidly near the peaks of the Na and Fe

layers [*Gardner and Liu, 2010; Gardner et al., 2005; Chen and Yi, 2011*]. For chemically active constituents such as Fe and Na, the fluctuations arise from purely dynamical effects associated with wave-induced displacement, as well as chemical effects associated with the perturbed production and loss reactions involving the species. The primary source of density fluctuations in the MLT is the vertical displacement associated with wave-induced vertical wind fluctuations. On the bottomsides of the Fe or Na layer, an upward displacement by the gravity wave winds transports a region of low Fe or Na density into a region of relatively high density. This results in a reduction, that is, a negative perturbation, in both constituents. In addition, due to the exponential decrease of the background atmosphere density with altitude, this same upward displacement of the whole atmosphere results in adiabatic cooling and a concomitant negative perturbation in the temperature. A downward

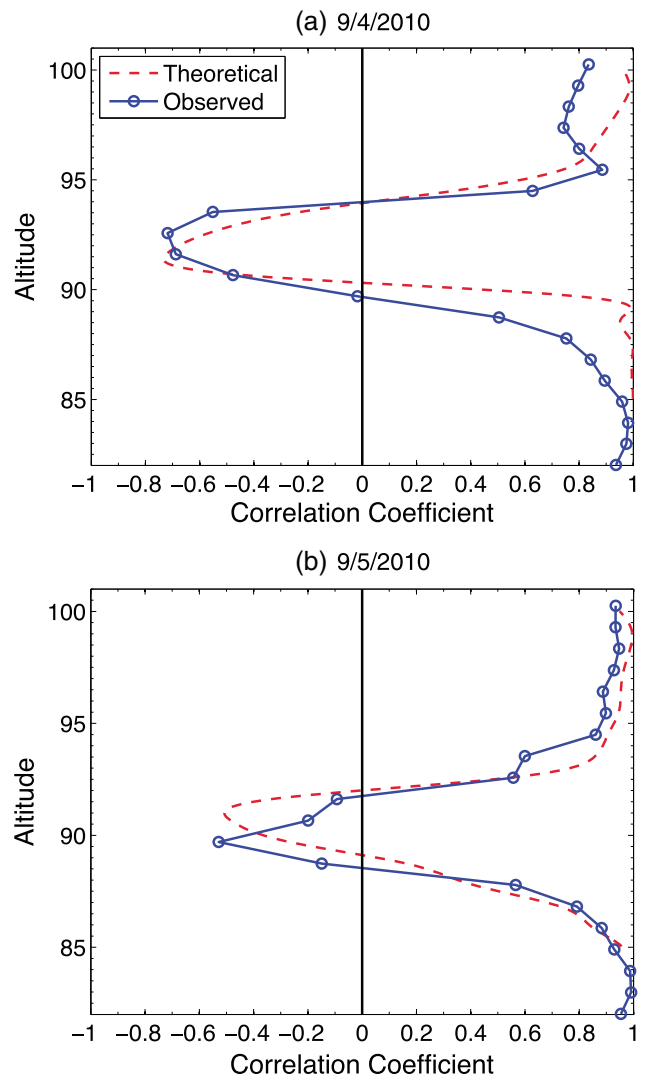


Figure 6. Theoretically calculated (dashed lines) and lidar-observed (solid lines) correlations between Fe and Na density perturbations on (a) 4 September and (b) 5 September 2010. Na temperatures are used in the theoretical calculations of Fe-Na correlations. The results using Fe temperatures are basically identical to the results shown here.

displacement by the winds on the layer bottomsides results in positive perturbations in both density and temperature. Hence, the temperature and Fe/Na perturbations are positively correlated on the layer bottomsides as observed in Figure 5. In addition, the Fe and Na fluctuations are correlated on the bottomsides of both layers, as observed in Figure 6, because downward (upward) advection leads to positive (negative) density perturbations in both species. In contrast, on the topside of a constituent layer, an upward displacement transports a region of high constituent density into a region of lower density, which results in a positive density perturbation and, as before, a negative temperature perturbation. Hence, on the topsides of both layers, the Fe and Na density fluctuations are positively correlated, but they are both negatively correlated (180° out of phase) with the temperature fluctuations (Figures 5 and 6). In the region between the Fe and Na layer peaks, the density perturbations of these two species are negatively correlated because this region corresponds to the topside of the Fe layer and the bottomsides of the Na layer.

[20] In the small region near the peaks of both layers, where the densities are approximately constant, the small wave-induced vertical displacements have little effect on the density fluctuations and so the relative Fe and Na variances are small, as observed in Figure 4. Off the layer peak, the large density gradients on both sides of the peak result in large relative Fe and Na variances under wave-induced vertical displacement, explaining the observed fast growth of variances near the layer top and bottom in Figure 4. In comparison, the background atmospheric density gradient is much smaller than those of Fe and Na off their peaks. Consequently, the vertical displacement induced by the same waves leads to small expansion/compression of the air parcels and thus limited adiabatic cooling/warming. The nonadiabatic heat exchange is also small because of the small gradient in the background temperature. Together, these factors explain why the observed relative temperature variances are significantly smaller than the relative Fe and Na variances off the layer peaks in Figure 4.

[21] It is worth to point out that the Fe/Na chemistry can reinforce the dynamical effects on the temperature-density correlations in the case of Fe and Na for the following reasons. On the bottomsides of the Fe/Na layer, the chemistry has a positive temperature dependence because the reactions involving atomic H that convert neutral reservoir species such as FeOH and NaHCO₃ back to their corresponding metal atoms have positive activation energies [Plane, 2003]. On the topside of the Fe/Na layer, the chemistry has a negative temperature dependence because the ion-molecule chemistry that converts Fe⁺ and Na⁺ ions back to neutral atoms involves forming molecular clusters, which is faster at lower temperatures [Plane, 2003]. In terms of the relative roles of dynamics and chemistry, dynamical perturbations operate on the timescale of the waves, whereas chemical perturbations induced by dynamics may have longer timescales. Therefore, the chemical responses can be damped, so not evident, when short-period waves are present.

4.2. Theoretical Studies and Comparison to Observations

[22] In reality, the situation is more complicated than this simple conceptual description because of nonlinear wave

effects, complex constituent profiles, and, of course, chemistry. However, because the Fe and Na density fluctuations are dominated by dynamics, it is possible to derive useful analytical models for the Fe and Na fluctuations and their covariance functions using the approach developed by Gardner and Liu [2010] for a spectrum of wind perturbations. The key derivations are summarized in Appendix A. The covariance between the temperature and constituent density fluctuations is given by

$$\overline{T'\rho'_C} = \frac{\text{Var}(T')\overline{\rho_C(z)}}{\gamma H(\Gamma_{\text{ad}} + \partial\overline{T}/\partial z)} \left[1 + \frac{\gamma H}{\overline{\rho_C(z)}} \frac{\partial\overline{\rho_C(z)}}{\partial z} \right]$$

$$\gamma H = \frac{\overline{T}}{(g/R - \Gamma_{\text{ad}})}, \quad (5)$$

where $\gamma \approx 1.4$ is the ratio of specific heats, $H = R\overline{T}/g \approx 5.6$ km is the pressure scale height of the background atmosphere, $\Gamma_{\text{ad}} = g/C_p \approx 9.5$ K/km is the adiabatic lapse rate, $g = 9.5$ m/s² is the acceleration of gravity, and $R = 287$ m²/K/s² is the gas constant of dry air. The prime denotes perturbation quantities and the overbar represents the sample mean. From equation (5), under the condition of $\Gamma_{\text{ad}} + \partial\overline{T}/\partial z > 0$, we can see that on the bottomsides of the constituent layer, where the scale height of the mean layer profile is positive, the covariance and associated correlation between the temperature and constituent fluctuations are positive. On the topside, where the constituent density scale height is negative and satisfies the inequality

$$H_C(z) = \left[\frac{1}{\overline{\rho_C(z)}} \frac{\partial\overline{\rho_C(z)}}{\partial z} \right]^{-1} < -\gamma H, \quad (6)$$

the temperature-density covariance is negative. The transition from positive to negative correlation occurs when the covariance $\overline{T'\rho'_C} = 0$, which corresponds to the condition of

$$\frac{\gamma H}{\overline{\rho_C(z)}} \frac{\partial\overline{\rho_C(z)}}{\partial z} = -1. \quad (7)$$

[23] Because the constituent scale height is infinite at the peak of the mean layer, such transition occurs several kilometers above the layer peak. For a Gaussian mean profile, the transition occurs at about $\sigma_C^2/\gamma H$ above the layer peak (σ_C is the RMS layer width given in Table 1) or about 2.5 km above the Fe layer peak and 2.3 km above the Na layer peak.

[24] The theoretical correlation and variance profiles were calculated for each night using equation (5) and other equations derived in Appendix A, by modeling the nightly mean Fe and Na layers as Gaussian distributions. The RMS layer widths were computed from the mean profiles plotted in Figure 3, and the layer peaks were computed by matching the altitudes where the observed temperature-density correlations are zero (Figure 5) to the theoretical model given by equations (5)–(7). The resulting theoretical models for (a) the Fe and Na relative variance profiles for 4 and 5 September are plotted in Figure 4, (b) the T -Fe and T -Na correlation profiles are plotted in Figure 5, and (c) the Fe-Na correlation profiles are plotted in Figure 6, along with the observational results.

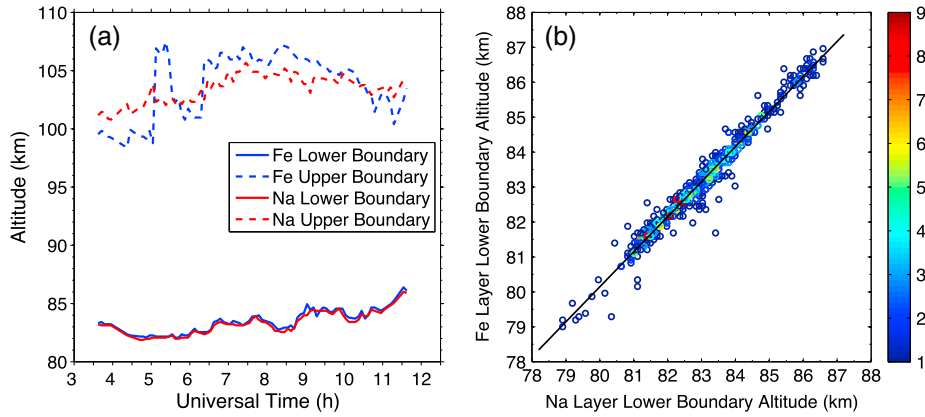


Figure 7. (a) Comparison of boundaries of Fe and Na layers on 4 September 2010; (b) scatterplot using all 12 nights of simultaneous Fe and Na lidar data to illustrate the relationship between Fe lower boundary (Z_{Fe}) and Na lower boundary (Z_{Na}). Here colors of blue to red indicate low to high occurrence frequencies and the numbers on the color bar show the number of occurrence. The black line is the linear regression fit to the data with equal weight to every point, $Z_{\text{Fe}} = 1.004 \times Z_{\text{Na}} - 0.136(\pm 0.584)$ (km).

[25] Figure 4 shows that the theoretical calculations have better agreement with the observations on 4 September than on 5 September 2010, and the agreement with Na is better than with Fe in general. This is very likely due to the different layer heights on these two nights and between two constituents. As will be discussed in section 5, the chemical “shelf” near 80 km consumes the metal layers rapidly below this shelf, forming a sharp layer bottom, thus deviating from a Gaussian distribution. Because the Na layer is peaking at higher altitude than the Fe layer, the Na profile deviates from the modeled Gaussian profile much less than the Fe profile. Also, the Na and Fe layers on 4 September are higher than those on 5 September. Therefore, the theoretical model gives better predictions on 4 September and on Na. The layer height difference may also explain the downward shifts of the transition points of temperature-density and $\rho'_{\text{Fe}}-\rho'_{\text{Na}}$ correlations on 5 September when compared to those on 4 September in Figures 5 and 6.

[26] Given that the Gaussian models are rough approximations to the mean Fe and Na profiles observed on these nights and chemical effects have been ignored, the theoretical variance and correlation models provide reasonably good descriptions of the altitude variations of the statistical relationships among the wave-induced temperature, Fe, and Na perturbations. These results provide strong support for the assumption that wave-induced dynamical effects are the dominant source of the Fe and Na density fluctuations.

5. Density Gradient in the Boundary Correlation

[27] A detailed study by *Yi et al.* [2008] from 26 nights of observations at Wuhan (30.5°N, 114.4°E), China, has found a close correlation between Fe and Na boundary altitude variations, especially at the layer bottomside. Our Table Mountain observations reveal similar behavior, with higher correlations at the lower boundary (nearly 99%) and slightly lower correlation (~70%) at the upper boundary. An example is shown in Figure 7a for 4 September 2012. Note that in the current study, the lower and upper boundaries of a metal layer are defined to be the altitudes where the densities are 2% of the nightly mean peak density, instead of a fixed

density for two lidars as presented in *Yi et al.* [2008]. For the total 704 pairs of Fe and Na density profiles over 12 nights, the Fe layer lower boundaries are plotted versus the Na lower boundaries in Figure 7b. The data exhibit a clear linear relationship with a correlation coefficient of 98.5%. This value is comparable to the correlation of 0.96 derived from the selected low-noise data in *Yi et al.* [2008]. Despite the different definitions of the metal layer boundaries, our observational results are strikingly similar to *Yi et al.* [2008], demonstrating the robustness of the strong correlation between Fe and Na lower boundaries.

[28] The observed boundary altitude correlations are consistent with the altitude-dependent correlation patterns shown in Figures 5 and 6, because the majority of lower boundaries fall in the altitude of 80–87 km where the correlations between Fe and Na density variations are large. Although the boundary altitude varies with time, it is still within the region of the large density gradient for both layers (below 87 km). As long as the dynamical response of the metal density to wave perturbations is dominant in this region of large density gradient, the Fe and Na layers will experience similar density variations in this region when subjected to the same wave perturbations, as discussed in section 4. The similar variations of Fe and Na densities lead to the similar movements of boundary altitudes and thus strong correlations between two metal layer boundaries.

[29] The larger gradient at the Fe and Na layer bottomside as compared to the topside has been characterized by *Chen and Yi* [2011] in great detail. This is also confirmed in our data. The nightly mean profiles plotted in Figure 3 show a much sharper gradient at the bottom than at the top. Furthermore, the gradient at the Fe bottomside is larger than that at the Na bottomside. This result is consistent with the previous reports [*Tilgner and von Zahn*, 1988; *Kane and Gardner*, 1993; *Chen and Yi*, 2011]. Here we present an explanation for this phenomenon. The metal layer bottom is formed when chemical reactions convert Fe and Na atoms to reservoir species around the altitude of 80 km. The reaction with O_3 is the first step in the conversion of Fe and Na to reservoir species, while atomic O and H are the main

constituents responsible for releasing Fe and Na atoms from their reservoirs. At night, a sharp transition of O and H mixing ratios occurs between 75 and 85 km, known as the “atomic oxygen shelf” [Plane, 2003], where the O and H mixing ratios decrease dramatically, over 5×10^5 times, from 85 to 75 km. The mixing ratio of O₃ also decreases, but only ~30 times from 90 to 80 km at night. Consequently, the neutral metal atoms are consumed rapidly below this shelf, forming a “sharp” layer bottom. Because the Fe layer peaks at 86.9 km, ~5.2 km lower than the Na peak at 92.1 km, the Fe peak is much closer to the shelf than the Na peak. As a consequence, the Fe density drops to nearly zero from a much larger density than the Na layer, forming a sharper bottom and thus a smaller scale height for Fe than for Na. There is no such chemical shelf at the layer topside, so the meteor ablation profile, molecular diffusion, and ion-molecule chemistry dominate the shape of the layer topside, leading to a much shallower density gradient for both species.

6. Conclusions

[30] The Fe Boltzmann and Na Doppler lidar observations at Boulder Table Mountain (40.13°N, 105.24°W), Colorado, in 2010 are analyzed for the first simultaneous study of correlations among the Fe layer, Na layer, and temperature in the MLT. We derive the accurate correlations by correcting the photon-noise-induced variance bias and eliminating the covariance bias via computing the cross correlations between Fe (Na) density and Na (Fe) temperature perturbations. This methodology provides a comprehensive process to real observational data in which noise is unavoidable. The correlation between Fe and Na density variations is positive below the Fe layer peak and above the Na peak where the Fe/Na density gradients have the same signs but becomes negative in between the Fe and Na peaks where the gradients are opposite. The large correlation between temperature and density fluctuations is positive on the layer bottomside but negative on the topside with the transitions occurring several kilometers above the layer peaks. Another new finding lies in the observed relative variances: The relative variances of Fe/Na densities reach minimum near the layer peaks but increase significantly toward the top and bottom edges. The relative temperature variance is comparable to the Fe/Na variances near the layer peaks but substantially smaller off the layer peaks.

[31] Qualitatively, these observational results are explained by hypothesizing that the wave-induced vertical displacement dominates the Fe/Na density perturbations in the MLT and by considering the different density gradients along the Fe/Na layer profiles and in the background atmosphere density, as detailed in section 4.1. Quantitatively, we theoretically derive the density response of the neutral atmosphere and of an atmospheric layer to a full spectrum of wave perturbations and obtain for the first time solutions for the covariance function between different constituents in the MLT and the temperature-density covariance function under the same wave perturbations. By modeling the nightly mean Fe and Na layers as simple Gaussian distributions, the observed correlation patterns can be largely reproduced by assuming that the density fluctuations are induced only by dynamical effects of waves while ignoring

the chemical effects. Such results provide strong support for the assumption that wave-induced dynamical effects (mainly the vertical displacement) are the dominant source of the short-term Fe and Na density fluctuations during a night. Note that with the current data, we cannot distinguish the nondissipating waves from the dissipating waves for inducing the vertical displacement.

[32] Comparison of the simultaneous 12 nights of lidar data reveals that the column abundance of Fe is ~3 times that of Na, the Fe centroid and peak altitudes are ~3 and 5 km lower than those of the Na, while Fe and Na layers have comparable RMS widths of ~4.3 km. These results are supportive of the previous observations made at other midlatitudes, although the ratio of the Fe/Na abundance in the Boulder case is slightly larger than that from earlier studies. Our observations at Boulder also confirm the strong correlation between the lower boundaries of the Fe and Na layers reported by Yi *et al.* [2008] and the larger density gradient of the Fe bottomside as compared to the Na bottomside reported by Chen and Yi [2011]. The lower boundary correlation is consistent with the correlation pattern discussed above because the lower boundary falls in the altitude range of 80–87 km with a large density gradient and is dominated by the linear response of metal densities to wave perturbations. We provide an explanation to the sharp density gradient at the metal layer bottomside in terms of the chemical shelf between 75 and 85 km. The Fe density peak is 5 km lower than the Na density peak and sits closer to the chemical shelf, where the consumption of neutral Fe and Na atoms rapidly increases with decreasing altitude due to the sharp decrease in mixing ratio of O and H. This produces the sharp density drop from the Fe density peak within a small altitude range near the layer bottom. Thus, the Fe layer bottomside in nighttime exhibits a sharper density gradient than the Na layer as observed.

[33] There are many other phenomena and mechanisms that can be studied from the simultaneous Fe/Na and temperature measurements, e.g., the interesting thermospheric metal layers and their relationship to the upper atmosphere chemistry, electrodynamics, and neutral dynamics. In addition, Doppler lidars are also capable of line of sight wind measurements. Such simultaneous and common-volume lidar measurements of Fe/Na density, temperature, and vertical wind provide new science opportunities, such as the derivation of Fe/Na flux and heat flux that can help study the constituent transport. These are the subjects in our future work.

Appendix A

[34] The density response of the neutral atmosphere or of an atmospheric layer composed of a neutral constituent is governed by the continuity equation,

$$\frac{\partial \rho_C}{\partial t} + \nabla \cdot (\rho_C \underline{V}) = P - L, \quad (\text{A1})$$

where ρ_C is the constituent density, \underline{V} is the velocity of the constituent, and P and L represent the production and loss terms. In this appendix the underline bars denote the vectors. When chemical effects and diffusion can be ignored

($P=L=0$) and the constituent is horizontally homogeneous, *Gardner and Shelton* [1985] have shown that the density response to wind perturbations can be written in the form

$$\rho_C(\underline{p}, t) = e^{-\chi} \rho_{C0}(z - \xi), \quad (\text{A2})$$

where $\rho_C(\underline{p}, t)$ is the perturbed density at position \underline{p} and time t and $\rho_{C0}(z)$ is the steady state density profile in the absence of wind perturbations. The parameters $\chi(\underline{p}, t)$ and $\xi(\underline{p}, t)$ are solutions to the partial differential equations

$$\frac{\partial \chi}{\partial t} = \nabla \cdot \underline{V} - \underline{V} \cdot \nabla \chi \quad (\text{A3})$$

$$\frac{\partial \xi}{\partial t} = w - \underline{V} \cdot \nabla \xi, \quad (\text{A4})$$

where the atmospheric velocity field is given by

$$\underline{V} = (\langle u \rangle + u')\hat{x} + (\langle v \rangle + v')\hat{y} + (\langle w \rangle + w')\hat{z}. \quad (\text{A5})$$

The parameters u , v , and w denote, respectively, the zonal, meridional, and vertical wind velocities with the angle brackets denoting the ensemble mean and the prime denoting the wind fluctuation.

[35] *Gardner and Shelton* [1985] and *Senft and Gardner* [1991] showed that the solutions to (A3) and (A4) are accurately represented by the equations

$$\chi(\underline{p}, t) \approx \int_{-\infty}^t \nabla \cdot \underline{V}' [x - (t - \tau)\langle u(z) \rangle, y - (t - \tau)\langle v(z) \rangle, z, \tau] d\tau \quad (\text{A6})$$

$$\xi(\underline{p}, t) \approx \int_{-\infty}^t w' [x - (t - \tau)\langle u(z) \rangle, y - (t - \tau)\langle v(z) \rangle, z, \tau] d\tau. \quad (\text{A7})$$

By expressing the unperturbed constituent number density in terms of its spatial Fourier transform $P_{C0}(\kappa)$, the perturbed density profile given by (A2) can be written as

$$\begin{aligned} \rho_{C0}(\underline{p}, t) &= \frac{1}{2\pi} \int_{-\infty}^{\infty} P_{C0}(\kappa) e^{-i\kappa z} d\kappa \\ P_{C0}(\kappa) &= \int_{-\infty}^{\infty} \rho_{C0}(z) e^{i\kappa z} dz \\ \rho_C(\underline{p}, t) &= \frac{1}{2\pi} \int_{-\infty}^{\infty} P_{C0}(\kappa) e^{-[\chi + i\kappa(z - \xi)]} d\kappa. \end{aligned} \quad (\text{A8})$$

The means, variances, and covariances follow directly from (A8):

$$\begin{aligned} \langle \rho_C(z) \rangle &= \frac{1}{2\pi} \int_{-\infty}^{\infty} P_{C0}(\kappa) \exp(-i\kappa z) \langle \exp(-\chi + i\kappa \xi) \rangle d\kappa \\ \langle T' \rho'_C \rangle &= \langle T' \rho_C \rangle = \frac{1}{2\pi} \int_{-\infty}^{\infty} P_{C0}(\kappa) \exp(-i\kappa z) \langle T' \exp(-\chi + i\kappa \xi) \rangle d\kappa \\ \langle \rho'_{\text{Na}} \rho'_{\text{Fe}} \rangle &= \langle \rho_{\text{Na}} \rho_{\text{Fe}} \rangle - \langle \rho_{\text{Na}} \rangle \langle \rho_{\text{Fe}} \rangle \\ \langle \rho_{\text{Na}} \rho_{\text{Fe}} \rangle &= \frac{1}{(2\pi)^2} \int_{-\infty}^{\infty} \int_{-\infty}^{\infty} P_{\text{Na}}(\kappa_1) P_{\text{Fe}}(\kappa_2) \\ &\exp[-i(\kappa_1 + \kappa_2)z] \langle \exp[-2\chi + i(\kappa_1 + \kappa_2)\xi] \rangle d\kappa_1 d\kappa_2. \end{aligned} \quad (\text{A9})$$

[36] To evaluate the expectations in (A9), we note that wind and temperature perturbations are Gaussian distributed [*Gardner and Yang*, 1998; *Gardner and Liu*, 2010]. Because χ and ξ are linearly related to the wind perturbations through (A6) and (A7), χ , ξ , and T' are jointly distributed Gaussian random processes. For jointly distributed Gaussian processes, (A9) becomes

$$\begin{aligned} \langle \rho_C(z) \rangle &= \frac{e^{\langle \chi^2 \rangle / 2}}{2\pi} \int_{-\infty}^{\infty} P_{C0}(\kappa) \exp\left(-\frac{1}{2}\kappa^2 \langle \xi^2 \rangle\right) \\ &\exp[-i\kappa(z + \langle \chi \xi \rangle)] d\kappa \\ \langle T' \rho'_C \rangle &= -\langle T' \chi \rangle \langle \rho_C(z) \rangle - \langle T' \xi \rangle \frac{\partial \langle \rho_C(z) \rangle}{\partial z} \end{aligned} \quad (\text{A10})$$

and

$$\begin{aligned} \langle \rho_{\text{Na}} \rho_{\text{Fe}} \rangle &= \frac{e^{\langle \chi^2 \rangle}}{(2\pi)^2} \int_{-\infty}^{\infty} \int_{-\infty}^{\infty} P_{\text{Na}}(\kappa_1) P_{\text{Fe}}(\kappa_2) \\ &\exp\left[-\frac{1}{2}(\kappa_1 + \kappa_2)^2 \langle \xi^2 \rangle\right] \\ &\exp[-i(\kappa_1 + \kappa_2)(z + 2\langle \chi \xi \rangle)] d\kappa_1 d\kappa_2. \end{aligned} \quad (\text{A11})$$

Notice that the Fe-Na covariance has a different form than the T -density covariance. That is because the constituent fluctuations are not Gaussian distributed while the temperature fluctuations are [*Gardner and Yang*, 1998].

[37] It is not difficult to show that

$$\begin{aligned} \chi &= \frac{-(g/R - \Gamma_{\text{ad}}) T'}{(\Gamma_{\text{ad}} + \partial \langle T \rangle / \partial z) \langle T \rangle} = \frac{-T'}{\gamma H (\Gamma_{\text{ad}} + \partial \langle T \rangle / \partial z)} \\ \xi &= \frac{-T'}{(\Gamma_{\text{ad}} + \partial \langle T \rangle / \partial z)}, \end{aligned} \quad (\text{A12})$$

where the parameters g , R , Γ_{ad} , γ , and H are defined in section 4 [*Gardner and Liu*, 2010] so that

$$\begin{aligned} \langle \chi^2 \rangle &= \frac{(g/R - \Gamma_{\text{ad}})^2 \text{Var}(T')}{(\Gamma_{\text{ad}} + \partial \langle T \rangle / \partial z)^2 \langle T \rangle^2} = \frac{\text{Var}(T')}{(\gamma H)^2 (\Gamma_{\text{ad}} + \partial \langle T \rangle / \partial z)^2} \\ \langle \xi^2 \rangle &= \frac{\text{Var}(T')}{(\Gamma_{\text{ad}} + \partial \langle T \rangle / \partial z)^2} \\ \langle \chi \xi \rangle &= \frac{(g/R - \Gamma_{\text{ad}}) \text{Var}(T')}{(\Gamma_{\text{ad}} + \partial \langle T \rangle / \partial z)^2 \langle T \rangle} = \frac{\text{Var}(T')}{\gamma H (\Gamma_{\text{ad}} + \partial \langle T \rangle / \partial z)^2} \end{aligned} \quad (\text{A13})$$

and the temperature-density covariance becomes

$$\langle T' \rho'_C \rangle = \frac{\text{Var}(T') \langle \rho_C(z) \rangle}{\gamma H (\Gamma_{\text{ad}} + \partial \langle T \rangle / \partial z)} \left[1 + \frac{\gamma H}{\langle \rho_C(z) \rangle} \frac{\partial \langle \rho_C(z) \rangle}{\partial z} \right]. \quad (\text{A14})$$

If the unperturbed constituent profiles can be modeled as Gaussian distributions with abundances A_C , A_{Fe} , and A_{Na} , centroid heights z_C , z_{Fe} , and z_{Na} , and RMS layer widths σ_C , σ_{Fe} , and σ_{Na} , then the mean and mean square perturbed

density profiles and the expected value of the product of the perturbed Fe and Na profiles given by (A10) and (A11) are

$$\begin{aligned}
 \langle \rho_C(z) \rangle &= \frac{A_C \exp(\langle \chi^2 \rangle / 2)}{\sqrt{2\pi(\sigma_C^2 + \langle \xi^2 \rangle)}} \exp \left[-\frac{(z - z_C + \langle \chi \xi \rangle)^2}{2(\sigma_C^2 + \langle \xi^2 \rangle)} \right] \\
 \langle \rho_C^2(z) \rangle &= \frac{A_C^2 \exp(2\langle \chi^2 \rangle)}{2\pi\sigma_C \sqrt{\sigma_C^2 + 2\langle \xi^2 \rangle}} \exp \left[-\frac{(z - z_C + 2\langle \chi \xi \rangle)^2}{\sigma_C^2 + 2\langle \xi^2 \rangle} \right] \\
 \langle \rho_{Na} \rho_{Fe} \rangle &= \frac{A_{Na} A_{Fe} \exp(2\langle \chi^2 \rangle)}{2\pi \sqrt{\sigma_{Na}^2 \sigma_{Fe}^2 + \langle \xi^2 \rangle (\sigma_{Na}^2 + \sigma_{Fe}^2)}} \cdot \\
 &\exp \left[-\frac{\sigma_{Fe}^2 (z - z_{Na} + 2\langle \chi \xi \rangle)^2 + \langle \xi^2 \rangle (z_{Na} - z_{Fe})^2 + \sigma_{Na}^2 (z - z_{Fe} + 2\langle \chi \xi \rangle)^2}{2[\sigma_{Na}^2 \sigma_{Fe}^2 + \langle \xi^2 \rangle (\sigma_{Na}^2 + \sigma_{Fe}^2)]} \right].
 \end{aligned}
 \tag{A15}$$

These results can now be used to compute theoretical models for the correlation coefficient and variance profiles in terms of the measured temperature variance profile and the observed Fe and Na layer parameters.

[38] **Acknowledgments.** We gratefully acknowledge Chiao-Yao She, Jeff Thayer, and Gary Swenson for lending critical instruments to the STAR lidar, Jonathan S. Friedman for valuable discussions, and Ian Dahlke for his assistance in developing the STAR lidar. We appreciate three anonymous reviewers for their valuable comments and suggestions. The Fe Boltzmann lidar work was supported by National Science Foundation (NSF) McMurdo grant ANT-0839091, and the STAR lidar work was supported by NSF CAREER grant ATM-0645584 and CRRL grants ATM-0545353 and AGS-1136272. This work was also supported by NSF grants AGS-1115725 and AGS-1115224.

References

- Arnold, K. S., and C. Y. She (2003), Metal fluorescence lidar (light detection and ranging) and the middle atmosphere, *Contemp. Phys.*, *44*(1), 35–49.
- Chen, L., and F. Yi (2011), Average properties and small-scale variations of the mesospheric Na and Fe layers as observed simultaneously by two closely collocated lidars at 30°N, *Ann. Geophys.*, *29*, 1,037–1,048, doi:10.5194/angeo-29-1037-2011.
- Chiu, Y. T., and B. K. Ching (1978), The response of atmospheric and lower ionosphere layer structures to gravity waves, *Geophys. Res. Lett.*, *5*(6), 539–542, doi:10.1029/GL0051006p00539.
- Chu, X., and G. Papen (2005), Resonance fluorescence lidar for measurements of the middle and upper atmosphere, in *Laser Remote Sensing*, edited by T. Fujii and T. Fukuchi, pp. 179–432, CRC Press, Boca Raton, Fla.
- Chu, X., W. Pan, G. Papen, C. S. Gardner, G. Swenson, and P. Jenniskens (2000), Characteristics of Fe ablation trails observed during the 1998 Leonid meteor shower, *Geophys. Res. Lett.*, *27*(13), 1,807–1,810, doi:10.1029/1999GL010756.
- Chu, X., W. Pan, G. Papen, C. S. Gardner, and J. A. Gelbwachs (2002), Fe Boltzmann temperature lidar: Design, error analysis, and first results from the North and South Poles, *Appl. Opt.*, *41*(21), 4,400–4,410, doi:10.1364/AO.41.004400.
- Chu, X., W. Huang, W. Fong, Z. Yu, Z. Wang, J. A. Smith, and C. S. Gardner (2011a), First lidar observations of polar mesospheric clouds and Fe temperatures at McMurdo (77.8°S, 166.7°E), Antarctica, *Geophys. Res. Lett.*, *38*, L16810, doi:10.1029/2011GL048373.
- Chu, X., Z. Yu, C. S. Gardner, C. Chen, and W. Fong (2011b), Lidar observations of neutral Fe layers and fast gravity waves in the thermosphere (110–155 km) at McMurdo (77.8°S, 166.7°E), Antarctica, *Geophys. Res. Lett.*, *38*, L23807, doi:10.1029/2011GL050016.
- Friedman, J. S., X. Chu, C. Brum, and X. Lu (2013), Observation of a thermospheric descending layer of neutral K over Arcicibo, *J. Atmos. Sol. Terr. Phys.*, doi:10.1016/j.jastp.2013.03.002.
- Gardner, C. S., and A. Z. Liu (2010), Wave-induced transport of atmospheric constituents and its effect on the mesospheric Na layer, *J. Geophys. Res.*, *115*, D20302, doi:10.1029/2010JD014140.
- Gardner, C. S., and J. D. Shelton (1985), Density response of neutral atmospheric layers to gravity wave perturbations, *J. Geophys. Res.*, *90*(A2), 1,745–1,754.
- Gardner, C. S., and W. Yang (1998), Measurements of the dynamical cooling rate associated with the vertical transport of heat by dissipating gravity waves in the mesopause region at the Starfire Optical Range, New Mexico, *J. Geophys. Res.*, *103*(D14), 16,909–916,926.
- Gardner, C. S., T. J. Kane, D. C. Senft, J. Qian, and G. C. Papen (1993), Simultaneous observations of sporadic E, Na, Fe, and Ca⁺ layers at

- Urbana, Illinois: Three case studies, *J. Geophys. Res.*, *98*(D9), 16,865–16,873, doi:10.1029/93JD01477.
- Gardner, C. S., G. C. Papen, X. Chu, and W. Pan (2001), First lidar observations of middle atmosphere temperatures, Fe densities, and polar mesospheric clouds over the North and South Poles, *Geophys. Res. Lett.*, *28*(7), 1,199–1,202.
- Gardner, C. S., J. M. C. Plane, W. Pan, T. Vondrak, B. J. Murray, and X. Chu (2005), Seasonal variations of the Na and Fe layers at the South Pole and their implications for the chemistry and general circulation of the polar mesosphere, *J. Geophys. Res.*, *110*, D10302, doi:10.1029/2004JD005670.
- Gardner, C. S., X. Chu, P. J. Espy, J. M. C. Plane, D. R. Marsh, and D. Janches (2011), Seasonal variations of the mesospheric Fe layer at Rothera, Antarctica (67.5°S, 68.0°W), *J. Geophys. Res.*, *116*, D02304, doi:10.1029/2010JD014655.
- Gelbwachs, J. A. (1994), Iron Boltzmann factor LIDAR: Proposed new remote-sensing technique for mesospheric temperature, *Appl. Opt.*, *33*(30), 7,151–7,156.
- Helmer, M., J. M. C. Plane, J. Qian, and C. S. Gardner (1998), A model of meteoric iron in the upper atmosphere, *J. Geophys. Res.*, *103*(D9), 10,913–10,925.
- Kane, T. J., and C. S. Gardner (1993), Structure and seasonal variability of the nighttime mesospheric Fe layer at midlatitudes, *J. Geophys. Res.*, *98*(D9), 16,875–16,886.
- Ma, Z., and F. Yi (2010), High-altitude sporadic metal atom layers observed with Na and Fe lidars at 30°N, *J. Atmos. Sol. Terr. Phys.*, *72*(5–6), 482–491.
- Marsh, D. R. (2011), Chemical-dynamical coupling in the mesosphere and lower thermosphere, in *Aeronomy of the Earth's Atmosphere and Ionosphere*, edited by M. A. Abdu, D. Pancheva, and A. Bhattacharyya, pp. 3–17, Springer, New York, doi:10.1007/978-94-007-0326-1_1.
- Plane, J. M. C. (2003), Atmospheric chemistry of meteoric metals, *Chem. Rev.*, *103*, 4,963–4,984.
- Plane, J. M. C. (2012), Cosmic dust in the Earth's atmosphere, *Chem. Soc. Rev.*, *41*, 6,507–6,518, doi:10.1039/C2CS35132C.
- Plane, J. M. C., C. S. Gardner, J. Yu, C. Y. She, R. R. Garcia, and H. C. Pumphrey (1999), Mesospheric Na layer at 40°N: Modeling and observations, *J. Geophys. Res.*, *104*(D3), 3,773–3,788, doi:10.1029/1998JD100015.
- Raizada, S., and C. A. Tepley (2003), Seasonal variation of mesospheric iron layers at Arcicibo: First results from low-latitudes, *Geophys. Res. Lett.*, *30*(2), 1082, doi:10.1029/2002GL016537.
- Senft, D. C., and C. S. Gardner (1991), Seasonal variability of gravity wave activity and spectra in the mesopause region at Urbana, *J. Geophys. Res.*, *96*(D9), 17,229–17,264, doi:10.1029/91JD01662.
- She, C. Y., J. R. Yu, H. Latifi, and R. E. Bills (1992), High-spectral-resolution fluorescence light detection and ranging for mesospheric sodium temperature measurements, *Appl. Opt.*, *31*(12), 2,095–2,106.
- She, C. Y., S. S. Chen, Z. L. Hu, J. Sherman, J. D. Vance, V. Vasoli, M. A. White, J. R. Yu, and D. A. Krueger (2000), Eight-year climatology of nocturnal temperature and sodium density in the mesopause region (80 to 105 km) over Fort Collins, CO (41°N, 105°W), *Geophys. Res. Lett.*, *27*(20), 3,289–3,292, doi:10.1029/2000GL003825.
- Smith, J. A., W. Fong, B. Roberts, W. Huang, and X. Chu (2012), Very high-resolution Na Doppler LIDAR at Boulder, Colorado, *Proceeding of the 26th International Laser Radar Conference*, pp. 151–154, Porto Heli, Greece, 25–29 June.
- States, R. J., and C. S. Gardner (1999), Structure of the mesospheric Na layer at 40°N latitude: Seasonal and diurnal variations, *J. Geophys. Res.*, *104*(D9), 11,783–11,789.
- Tilgner, C., and U. von Zahn (1988), Average properties of the sodium density distribution as observed at 69°N latitude in winter, *J. Geophys. Res.*, *93*(D7), 8,439–8,454.
- Tsuda, T. T., X. Chu, T. Nakamura, M. K. Ejiri, and T. Kawahara (2012), Sodium layer in the thermosphere (110–130 km) observed at Syowa Station (69.0°S, 39.6°E) in Antarctica, American Geophysical Union Fall Meeting, San Francisco, California, 3–7 Dec.
- Wang, J., Y. Yang, X. Chen, G. Yang, S. Song and S. Gong (2012), Double sodium layers observation over Beijing, China, *Geophys. Res. Lett.*, *39*, L15801, doi:10.1029/2012GL052134.
- Wang, Z., X. Chu, W. Huang, W. Fong, J. A. Smith, and B. Roberts (2012), Refurbishment and upgrade of Fe Boltzmann/Rayleigh temperature lidar at Boulder for McMurdo lidar campaign in Antarctica, *Proceeding of the 26th International Laser Radar Conference*, pp. 207–211, Porto Heli, Greece, 25–29 June.
- Yi, F., S. Zhang, X. Yue, Y. He, C. Yu, C. Huang, and W. Li (2008), Some ubiquitous features of the mesospheric Fe and Na layer borders from simultaneous and common-volume Fe and Na lidar observations, *J. Geophys. Res.*, *113*(A4), A04S91, doi:10.1029/2007JA012632.
- Yi, F., C. Yu, S. Zhang, X. Yue, Y. He, C. Huang, Y. Zhang, and K. Huang (2009), Seasonal variations of the nocturnal mesospheric Na and Fe layers at 30°N, *J. Geophys. Res.*, *114*(D1), D01301, doi:10.1029/2008JD010344.